

Charge order and antiferromagnetism in the extended Hubbard model

Joseph Paki,¹ Hanna Terletska,² Sergei Isakov,¹ and Emanuel Gull^{1,3}

¹*Department of Physics, University of Michigan, Ann Arbor, Michigan 48109, USA*

²*Department of Physics and Astronomy, Computational Science Program, Middle Tennessee State University, Murfreesboro, Tennessee 37132, USA*

³*Center for Computational Quantum Physics, Flatiron Institute, New York, New York 10010, USA*



(Received 3 April 2019; revised manuscript received 4 June 2019; published 25 June 2019)

We study the extended Hubbard model on a two-dimensional half-filled square lattice using the dynamical cluster approximation. We present results on the phase boundaries between the paramagnetic metallic (normal) state and the insulating antiferromagnetic state, as well as between the antiferromagnetic and charge-order states. We find hysteresis along the antiferromagnet/charge order and normal/charge-order phase boundaries (at larger values of the on-site interaction), indicating first-order phase transitions. We show that nearest-neighbor interactions lower the critical temperature for the antiferromagnetic phase. We also present results for the effect of nearest-neighbor interactions on the antiferromagnetic phase boundary and for the evolution of spectral functions and energetics across the phase transitions.

DOI: [10.1103/PhysRevB.99.245146](https://doi.org/10.1103/PhysRevB.99.245146)

I. INTRODUCTION

Strongly correlated electron systems with many degrees of freedom often exhibit complex phase diagrams with a wide range of phases [1]. Competing interactions may lead to symmetry-breaking charge, spin, superconducting, or orbital ordered states. Of special interest are systems that display several ordered states in close proximity, such as charge order and magnetism, as other types of orders (such as superconductivity) often occur near their respective phase boundaries.

Compounds that exhibit both charge-ordered (CO) and antiferromagnetic (AFM) phases are ubiquitous in nature [1–3]. Examples include the *d*-electron material $\text{La}_{1-x}\text{Sr}_x\text{FeO}_3$ [4], the doped nickelate $\text{La}_{2-x}\text{Sr}_x\text{NiO}_4$ [5], the layered manganite $\text{La}_{0.5}\text{Sr}_{1.5}\text{MnO}_4$ [6], the cobalt oxides [7], the doped iridate [8], the layered ruthenate [9], and the layered cuprates $\text{La}_{2-x}\text{Sr}_x\text{CuO}_4$ and $\text{La}_{2-x}\text{Ba}_x\text{CuO}_4$ at 1/8 doping [10]. Organic salts, including the one-dimensional $(\text{TMTTF})_2\text{SbF}_6$ [11–14] and two-dimensional (2D) quarter-filled compounds [15–17] similarly show coexisting AFM and CO. Several of these materials are also superconducting. Understanding the phase diagram in these materials requires a detailed analysis of the competition between these two types of ordering.

Fermion model systems aim to capture the main aspects of these materials while abstracting the complexity of the underlying electronic structure problem. The most simple of these models is the Hubbard model in two dimensions, which has become the archetype of strongly correlated electron systems [18]. The model approximates the band structure by a single band with nearest-neighbor hopping t and on-site interaction U . It is known to have both strong short-ranged AFM correlations [19–22] and a CO ground state at $\frac{1}{8}$ doping [23].

While CO in the 2D Hubbard model on a square lattice is rather fragile, the extended Hubbard model promotes CO by the explicit addition of a repulsive nearest-neighbor

interaction term V . The nonlocal interactions have been found to be sizable in a number of low-dimensional materials, resulting in CO as well as strong screening effects [24–28]. The inclusion of nonlocal intersite interactions energetically favors breaking translational symmetry and generating checkerboard CO states with two electrons on one site, none on its nearest neighbors, and a repeating (π, π) CO pattern [29]. In contrast, a large on-site interaction U will enhance AFM (π, π) correlations [30]. The interplay between intersite interaction V , local interaction U , temperature, and doping effects thereby generates the rich phase diagram of the model.

The extended Hubbard model has been of interest both as a proxy for the exploration of charge order caused by electron repulsion [24,25,27,29,31–50] and as a model system for testing the effect of nonlocal interactions on electron correlations [51–55]. In that context, it has been particularly valuable to illustrate the convergence of diagrammatic extensions of the dynamical mean field theory [56,57] (DMFT), including the GW+DMFT [34,35,58] and the dual boson approximation [46,59–62].

Real materials that exhibit CO in the vicinity of AFM are considerably more complex than the simple extended Hubbard model. Nevertheless, there is merit in identifying model systems and nonperturbative approximations in which those phases occur in close proximity, as simple competition effects such as the one between local and nonlocal interactions here can provide general guiding principles for understanding their overall behavior.

In this paper, we study the interplay between CO and AFM in the 2D half-filled extended Hubbard model at nonzero temperature using the dynamical cluster approximation (DCA) [63,64] on an eight-site cluster. This nonperturbative numerical method allows the explicit inclusion of nonlocal interactions and correlations and treats charge and spin correlations on equal footing. Previous DCA work in the absence of AFM order showed the detailed finite temperature phase diagram

at [49] and away from [50] half-filling, demonstrating that an increase of V at fixed U leads to a checkerboard pattern of electrons characterized by a staggered density. This phase appears below a critical temperature which strongly depends on U and V . We also found that nonlocal interactions cause noticeable screening effects. Our study extends this work by allowing for both AFM and CO. This allows us to explore finite temperature phase transitions between AFM and CO and illustrate the effect of nonlocal interactions on the AFM phase.

The exact mathematical solution of the Hubbard model does not support AFM order at nonzero temperature, as long-ranged AFM fluctuations will always destroy this order [65]. However, many numerical methods such as the DCA operate on a finite system and thereby truncate the correlation length, either suppressing longer ranged fluctuations entirely or supplanting them by infinitely ranged order [64,66–71]. In our paper, we use this truncation to generate a system that exhibit both CO and AFM to study the generic interplay between those phases.

The remainder of this paper is organized as follows. In Sec. II, we discuss the Hamiltonian, our approximation, and the numerical method we use. In Sec. III, we present and discuss our results. We first show the phase diagrams in the space of $T - V$ and $V - U$. We then explore the corresponding CO and AFM order parameters and their temperature T and nonlocal interaction V dependence, as well as the details of the phase boundaries (Sec. III C). Finally, we discuss the energetics (Sec. III D) across the phase transitions, the hysteresis behavior (Sec. III E), and the evolution of spectral functions (Sec. III F) across the phase boundaries. We present our conclusions in Sec. IV.

II. MODEL AND METHODS

This paper applies the methods developed in Refs. [30,49] to study the formation and competition between AFM and CO phases in the half-filled 2D extended Hubbard model on a square lattice. The following provides an overview of the formalism, and the interested reader is referred to Ref. [49] for further details.

The Hamiltonian for the extended Hubbard model on a 2D square lattice is given by

$$H = -t \sum_{\langle ij \rangle, \sigma} (c_{i\sigma}^\dagger c_{j\sigma} + c_{j\sigma}^\dagger c_{i\sigma}) + U \sum_i n_{i\uparrow} n_{i\downarrow} + \frac{V}{2} \sum_{\langle ij \rangle, \sigma\sigma'} n_{i\sigma} n_{j\sigma'} - \tilde{\mu} \sum_{i\sigma} n_{i\sigma}, \quad (1)$$

where t is the nearest-neighbor hopping amplitude, U and V represent the on-site and nearest-neighbor Coulomb interactions, and $\tilde{\mu}$ denotes the chemical potential. $c_{i\sigma}^\dagger$ ($c_{i\sigma}$) is the creation (annihilation) operator for a particle with spin σ on lattice site i , and the particle number operator for site i is $n_{i\sigma} = c_{i\sigma}^\dagger c_{i\sigma}$. Throughout this paper, we restrict our attention to the half-filled system, which occurs at $\tilde{\mu} = \mu_{\text{HF}} = \frac{U}{2} + 4V$ for the 2D square lattice. We use dimensionless units U/t , V/t , βt , and μ/t , and set $t = 1$.

We compute our results within the DCA [63,64] to find approximate solutions for the lattice model. The DCA is a cluster extension of the DMFT [72] that approximates

the infinite lattice problem by a finite size cluster coupled to a noninteracting bath. The coupling to the bath is adjusted self-consistently by coarse graining the Brillouin zone into N_c momentum space patches. The self-consistency condition requires that certain cluster quantities (such as the Green's function) match the corresponding coarse-grained lattice quantities [64]. The scheme becomes exact in the limit where $N_c \rightarrow \infty$, and recovers DMFT for $N_c = 1$. The method is able to describe short-ranged spatial correlations nonperturbatively (i.e., correlations on length scales smaller than N_c), but correlations outside the cluster are neglected. The method is also capable of simulating ordered phases, as long as the symmetry breaking is commensurate with the cluster [30,64]. An important detail is that for the extended Hubbard model, the DCA coarse-graining procedure renormalizes the nearest-neighbor interaction V as $\bar{V} = \sin(\pi/N_c)/(\pi/N_c)V$, as described by Refs. [33,73]. In this paper, we study systems with $N_c = 8$.

We can bias the system towards an ordered phase by adding symmetry breaking terms to the Hamiltonian [30,49,64]. These terms extend Eq. (1) by a staggered chemical potential $\mu_i = \mu_0 e^{iQr_i}$ and/or a staggered magnetic field $h_i = h_0 e^{iQr_i}$, with $(Q = (\pi, \pi))$ for both AFM and checkerboard CO),

$$H_{\mu_0, h_0} = H + \sum_{i\sigma} \mu_i n_{i\sigma} + \sum_i h_i m_i; \quad (2)$$

here $m_i = n_{i,\uparrow} - n_{i,\downarrow}$. The staggered chemical potential and magnetic field break the translational symmetry and divide the original bipartite lattice into two sublattices A and B , thereby doubling the unit cell. In this paper, we begin simulations with a small $\mu_0/t \approx 0.05$ or $h_0/t \approx 0.05$ on the first iteration and then set these quantities to zero on subsequent iterations. The system is then allowed to evolve freely, and will either converge to a paramagnetic state (electrons uniformly distributed over lattice site and spin) or fall into one of the ordered states.

Solving the cluster impurity problem requires the use of a quantum impurity solver. Here we use the continuous time auxiliary field quantum Monte Carlo algorithm (CTAUX) [74–76], modified to accommodate nonlocal density-density interactions [49,50].

A. Green's functions

The ordered phases investigated here reduce the translation symmetry of the lattice [64]. This doubles the size of the unit cell in real space while halving the size of the Brillouin zone, such that in the ordered phase the momentum space points k and $k + Q$ become degenerate, where for AFM and CO $Q = (\pi, \pi)$. To study ordered and nonordered phases with the same method, a double cell formalism is used in which momentum space Green's functions take on a block diagonal structure. Each block takes on the form

$$G_\sigma(k, i\omega_n) = \begin{pmatrix} G_\sigma(k, k; i\omega_n) & G_\sigma(k, k + Q; i\omega_n) \\ G_\sigma(k + Q, k; i\omega_n) & G_\sigma(k + Q, k + Q; i\omega_n) \end{pmatrix}, \quad (3)$$

where $\omega_n = (2n + 1)\pi/\beta$ with $\beta = 1/k_B T$ denotes the fermionic Matsubara frequencies. In the absence of order $G_\sigma(k, k + Q) = G_\sigma(k + Q, k) = 0$ [30,49], so the Green's functions become diagonal in momentum space. In the

ordered phases, these off-diagonal components become finite and obey symmetry relations. For AFM, $G_\sigma(k, k+Q) = G_\sigma(k+Q, k) = -G_{-\sigma}^*(k, k+Q) = -G_{-\sigma}^*(k+Q, k)$, while for CO we have $G_\sigma(k, k+Q) = G_\sigma(k+Q, k) = G_{-\sigma}(k, k+Q) = G_{-\sigma}(k+Q, k)$. Here on, for a short-hand notation we drop the frequency index. We can define both the momentum dependent and local sublattice and spin-resolved Green's functions as follows (denoting the two sublattices as A and B) [49]:

$$G_{A/B,\sigma}(k) = \frac{G_\sigma(k, k) + G_\sigma(k+Q, k+Q)}{2} \pm G_\sigma(k, k+Q) \quad (4)$$

$$G_{A/B,\sigma}^{\text{loc}} = \frac{1}{N_c} \sum_k G_{A/B,\sigma}(k). \quad (5)$$

Similar equations describe the sublattice resolved self-energies. These quantities allow us to study how the density of states (from analytic continuation of $G_{A/B,\sigma}^{\text{loc}}$) and self-energies behave on each sublattice.

B. Order parameter

The order parameters for charge order, Δ_{CO} , and antiferromagnetism, Δ_{AFM} , can be computed from the spin-resolved cluster site densities, $n_{i\sigma}$:

$$\Delta_{\text{CO}} = \frac{2}{N_c} \left| \sum_{i \in A, \sigma} n_{i\sigma} - \sum_{i \in B, \sigma} n_{i\sigma} \right|, \quad (6)$$

$$\Delta_{\text{AFM}} = \frac{1}{N_c} \left| \sum_i e^{iQr_i} (n_{i\uparrow} - n_{i\downarrow}) \right|. \quad (7)$$

The factor of 2 in Eq. (6) arises because the sums in this expression are only over half the sites in the lattice, i.e., over the sites in each sublattice. These expressions can also be written in terms of the off-diagonal components of the momentum space Green's function in imaginary time, $G_{k,k+Q,\sigma}(\tau)$ [64]:

$$\Delta_{\text{CO}} = \frac{2}{N_c} \left| \sum_{k\sigma} G_\sigma(k, k+Q; \tau=0^-) \right|, \quad (8)$$

$$\Delta_{\text{AFM}} = \frac{1}{N_c} \left| \sum_k (G_\uparrow(k, k+Q; \tau=0^-) - G_\downarrow(k, k+Q; \tau=0^-)) \right|. \quad (9)$$

III. RESULTS

We present the dependence of phase boundaries, order parameters, and of the energetics on U , V , and T for the half-filled extended Hubbard model. We focus on three phase boundaries exhibited by the model in our approximation: those between the nonordered paramagnetic (normal) and AFM phases (normal AFM), normal and CO phases (normal CO), and AFM and CO phases (AFM CO). In Sec. III A, we present the $T-V$ phase diagram (at $U=4t$) for the model and examine how the order parameters and energetics behave along cuts through the different phase boundaries. We

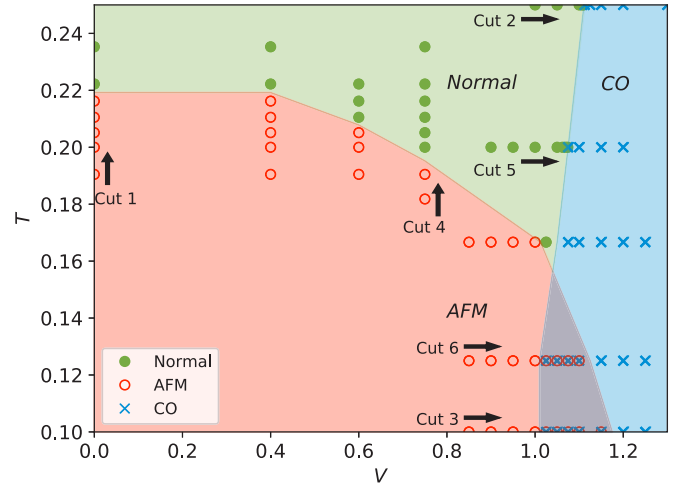


FIG. 1. $T-V$ phase diagram for the half-filled extended Hubbard model at $U=4$. Green shading and filled circles represent normal (paramagnetic) state. Red area and open circles represent region with AFM ordering. Blue area and crosses depict the CO state. Region with both crosses and circles shows the first-order CO/AFM coexistence. Symbols denote simulation points. Transition lines are obtained from the midpoint between simulation points. Also indicated are six phase transition cuts referred to in the text.

also demonstrate hysteresis across the AFM CO and normal-CO phase boundaries, indicating first-order transitions. In Sec. III B, we present the temperature dependence of the $V-U$ phase diagram, comparing temperatures $T/t = 1/6$ and $T/t = 1/10$.

A. $T-V$ phase diagram

The phase diagram as a function of nearest-neighbor interaction V and temperature T at fixed $U/t = 4$ is shown in Fig. 1. The model exhibits a paramagnetic metallic phase (from now on referred to as the normal state) at high temperature and weak V (green shading/filled circles in Fig. 1), an AFM (red shading/open circles) at low temperature and low V , and a CO state at large V (blue shading/crosses). Symbols indicate simulation points; the phase transition boundaries are obtained from the midpoint between simulation results in different phases.

As is expected from Hubbard model simulations in the absence of V , strong AFM correlations exist at half filling. In cluster DMFT simulations, these cause the system to polarize and fall into a long-range antiferromagnetically ordered phase [64,68] below a transition temperature of $T \sim 0.22$ (at $V=0$). This “phase” is an artifact of the approximation and should be understood as an area where long-ranged AFM fluctuations are strong [64].

Larger DCA clusters will eventually lead to a suppression of AFM order in 2D and simply exhibit strong AFM fluctuations [64]. The AFM correlation length is large compared to accessible cluster sizes (and rapidly growing as temperature is decreased), making observing a true paramagnetic state difficult within this approximation [64]. However, one may expect that effects present in real systems but excluded from the Hubbard model, such as inter-layer couplings, disorder,

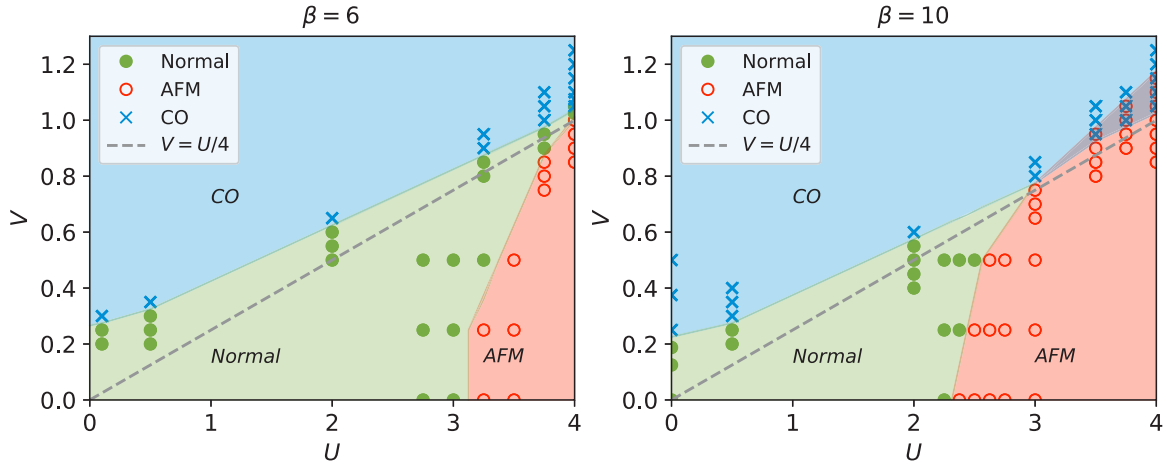


FIG. 2. Comparison of the $U - V$ phase diagram of the extended Hubbard model at inverse temperature $\beta = 6/t$ and $\beta = 10/t$, both at $\mu = 0$. At high temperature (left panel) the AFM and CO phases are entirely separated by the normal state region for this range of U . Upon lowering T , a hysteresis region emerges at larger U in which both the CO and AFM solutions are stable. Points with both blue crosses and red open circles indicate points at which the simulation converges to either a CO or AFM solution, depending on whether a CO or AFM starting solution is used. The mean-field result (dashed line) for the phase boundary between the normal and CO state, $V = U/4$, is also shown.

band-structure effects, and longer ranged Coulomb interactions may stabilize these fluctuations and lead to an actual phase transition with similar overall behavior.

Nonlocal interactions V suppress these fluctuations. We find that as we increase V above $\sim 0.6t$, the critical temperature of the AFM phase is rapidly reduced. Within DCA, further increase of V will entirely suppress the AFM state, so beyond a value of $\sim 1.2t$ no AFM ordering is observed in our calculations.

Repulsive nonlocal interactions on a bipartite lattice eventually lead to a CO state [49]. For our parameters, at $U/t = 4$, this charge ordering sets in at $V/t \sim 1.1$ for the highest T shown. Lowering the temperature shifts that phase boundary toward lower values of U , such that at $T/t = 0.1$ the phase boundary is observed near $V/t = 1.0$.

For the parameter values chosen, there is an area where both CO and AFM states can occur. In this area, the nearest-neighbor interaction V is large enough that CO is favorable, but the temperature is low enough that AFM fluctuations are strong. In our simulation, we find a first-order coexistence regime where the system is either in a CO state (where magnetic order is absent) or in an AFM state (where charge order is absent). Plots of the real part of the self-energy for frequency going to infinity for all the cuts in Fig. 1 are shown in the Supplemental Material [77].

B. V - U phase diagram

To illustrate the evolution of the phase diagram as a function of U and V , we present cuts in the V - U plane at constant temperature in Fig. 2. The left panel shows $T/t = 1/6$, the right panel $T/t = 1/10$. At large V , the system is CO at half-filling (blue area). At small V but large U , the system undergoes an AFM transition in this approximation (red area). And at small U and V , the model is in an isotropic “normal” state (green).

As explored in previous work [49,50] (see also results from other methods [34,46,78–80]), the CO transition occurs above

the mean-field line $V = U/4$ [81], has a nonzero intercept at $U = 0$, and is only weakly temperature dependent. The critical value of V at which the transition to the CO occurs increases with temperature [29]. In contrast, the AFM phase in this approximation is very strongly temperature dependent for these parameters, hinting at a rapid evolution of the spin susceptibility in this model, and moves to substantially lower U and larger V as the temperature is lowered (compare to the right panel).

At the lower temperature, the coexistence between the two phases occurs at large V and large U , where the nonlocal interaction is strong enough to favor CO but the local U also permits long-range AFM.

C. Order parameter and phase boundaries

CO is characterized by a difference between the occupancies on different sublattices, as described by the order parameter in Eq. (6). AFM, as defined by the order parameter of Eq. (7), is identified by different occupancies of the two spin species. To distinguish between ordered and isotropic points in the presence of Monte Carlo noise, we define simulation points with order parameters larger than 0.1 as ordered in Figs. 1 and 2.

Raw data for the order parameters along the cuts indicated in Fig. 1 are shown in Fig. 3. The bottom left panel shows the order parameters across the AFM to the normal-state phase boundary. Shown are two cuts at constant V but for varying temperature. As expected, this phase transition is second order [49]. Larger nonlocal interaction $V = 0.75t$ moves the onset of the phase transition to lower temperatures, suppressing both the onset and the strength of the AFM order parameter.

The top left panel shows the transition from the normal state to CO, at constant temperature T , as a function of V . The CO phase is identified by a nonzero staggered density appearing at larger values of V . In the absence of long-ranged AFM order, this transition has been analyzed in detail in previous work [49]. As discussed later on in Sec. III E, at larger

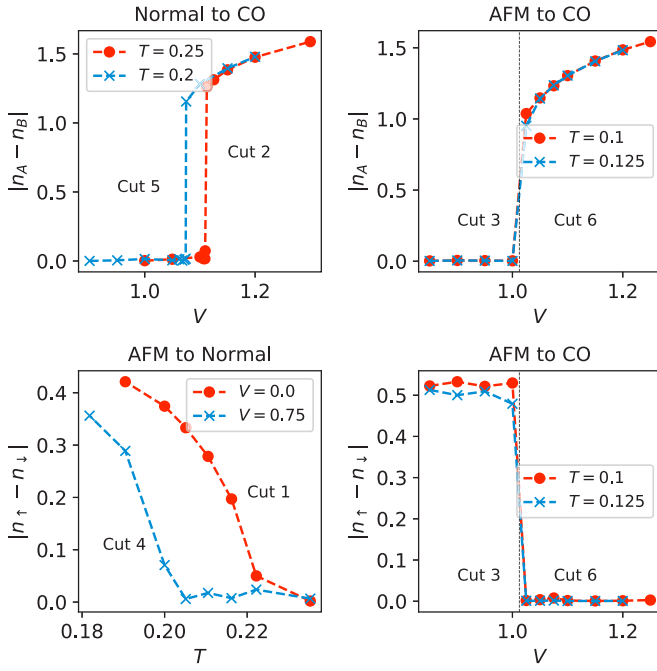


FIG. 3. AFM and CO order parameters across phase transition. $U/t = 4$, $\mu = 0$. Normal CO at constant T (top left panel), AFM normal at constant V (bottom left panel), and AFM CO (right panels). AFM-CO cuts are obtained with a CO starting solution; see Fig. 5 for hysteresis. Errors on the order of symbol size.

values of local interactions U , we find this transition to be the first-order transition [32,52,55] with a characteristic hysteresis behavior of the order parameter. Lower temperatures lead to an earlier onset of the CO state at lower V [49].

The right two panels show the order parameter across the transition from the AFM (low V) to the CO (large V) states, at constant T as a function of V . Shown are both the magnetic (bottom) and CO (top) order parameters. This transition is first order (see Sec. III E for hysteresis); shown here are data obtained by starting from a CO solution.

In other works [27,60], it has been suggested that the phase diagram in the $U - V$ plane may be approximately described by lines with constant U^* . In this context, the lack of dependence of the weak- V phase-transition line on V suggests that this method does not provide a suitable description of the location of the phase transition line. Whether another simple single-valued parameter (e.g., chosen along the lines of Ref. [82]) may provide an accurate description of these lines, and whether any of the prescriptions in Refs. [27,60,82] yield accurate results for quantities other than the AFM phase transition line, is an open question.

D. Energetics

Figure 4 shows the contributions to the energetics as the system crosses the phase boundaries. Shown are the total energy H_{Total} , the kinetic energy H_{KE} , the contribution of the local energy to the interaction energy H_U , and the contribution

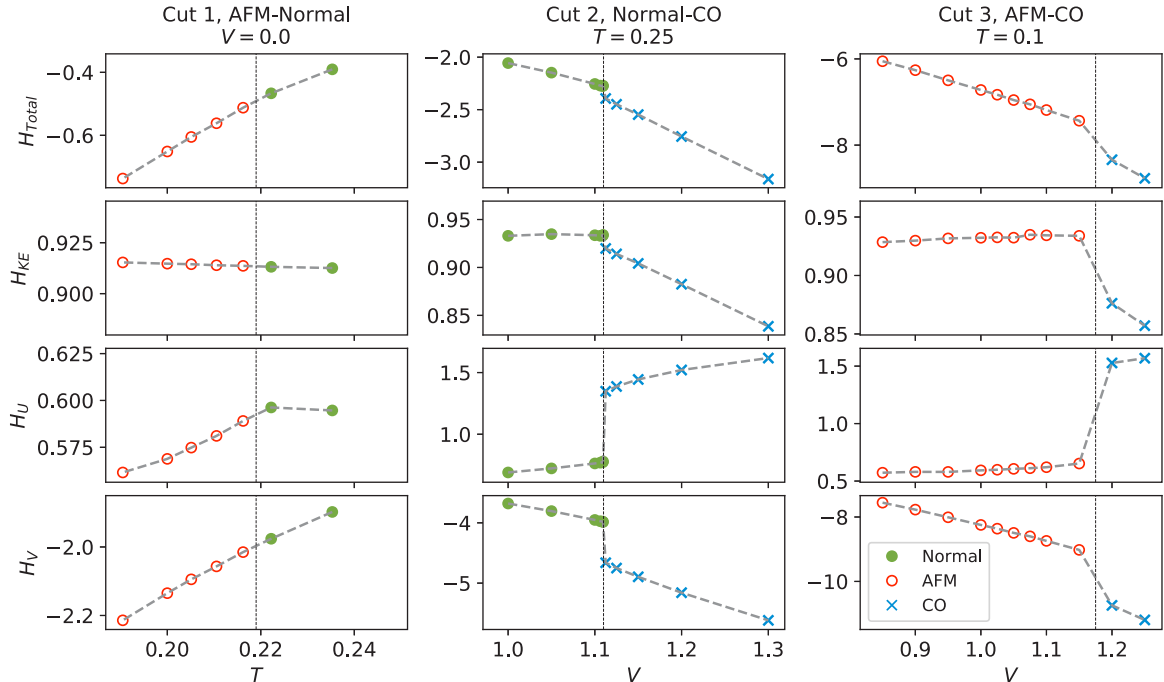


FIG. 4. Contribution to the energetics across three phase transitions for the extended Hubbard model at $U = 4$, $\mu = 0$. Left column: AFM-normal transition along cut 1 from Fig. 1. As AFM order emerges at lowering temperature, the on-site interaction energy, H_U , is suppressed by the reduction in double occupancy. Middle column: Normal-CO transition along cut 2 from Fig. 1. The localization of electrons on the one sublattice leads to a decrease in the kinetic energy, H_{KE} , an increase in the on-site interaction energy, H_U , in exchange for a decrease in the nearest-neighbor interaction energy, H_V . Right column: AFM-CO transition along cut 3 from Fig. 1, showing only the results obtained from the AFM starting solution. An increase in the on-site interaction energy, H_U , is exchanged for a decrease in the nearest-neighbor interaction energy, H_V . The symbols for each data point, indicating the stable phase, follow from Fig. 1. Errors on the order of symbol size.

of the nonlocal term to the interaction energy H_V . These energies are computed as [76,83]

$$H_{KE} = \frac{1}{N_C} \sum_{k\sigma} (\epsilon_k - \tilde{\mu}) \langle n_{k\sigma} \rangle, \quad (10)$$

$$H_V = \frac{K - \langle k \rangle}{\beta N_C} - H_U, \quad (11)$$

$$H_U = \frac{U}{N_C} \sum_i \langle n_{i\uparrow} n_{i\downarrow} \rangle, \quad (12)$$

and $H_{\text{Total}} = H_{KE} + H_U + H_V$. $\epsilon_k = -2t(\cos k_x + \cos k_y)$ is the dispersion on the 2D square lattice, $\langle k \rangle$ denotes the average order sampled during the Monte Carlo simulation [76,83], and K is a constant introduced in the CTAUX algorithm by a Hubbard-Stratonovich transformation [74].

The first column of Fig. 4 shows how the different energy components change as the temperature is increased and the system moves from an AFM ordered phase to the normal state. The dominant change upon entering the AFM phase is a reduction of the on-site interaction, H_U , due to the suppression of the double occupancy. Kinetic energies and potential energies show little change across the transition. This is consistent with the AFM transition in single-site DMFT and four-site cluster DMFT below the Mott transition, where the opening of the AFM gap lowers the energy by suppressing the double occupancy [84].

The second column shows the energetics as V is increased and the system enters the CO state from the normal state at high temperature ($T = 0.25$). Here, the major change in the energetics is the nonlocal interaction energy term H_V , which can be dramatically lowered by entering a CO phase. The kinetic energy decreases slightly as electrons become constrained to one sublattice, and the transition is accompanied by an increase in the on-site interaction energy, H_U , caused by the increase of the double occupancy in the CO state. The sharp jump in energies across the transition is consistent with the first-order transition across this cut.

Finally, the third column displays the evolution of the system across AFM-CO transition at lower temperature $T = 0.1$. The transition is the first order with a very pronounced jump in energy changes across the phase boundaries. The data shown is from the branch of the hysteresis that starts in the AFM phase. It is evident that the transition requires a substantial rearrangement of the energetics, with major changes in all energy terms.

The slope of the charge-order phase transition line shows that our entropic contribution is consistent with the ordered insulator having a lower entropy than the metallic state [85]. A detailed analysis of the entropic contribution to the competition between the ordered states would require thermodynamic integration on a fine grid [86,87], which we leave for later study.

E. Hysteresis

We present evidence of hysteresis in the AFM/CO transition at low temperatures in Fig. 5. This data is obtained by running each simulation point twice—once with an initial configuration corresponding to an AFM ordered state, and once with one describing a CO state. Outside the coexistence

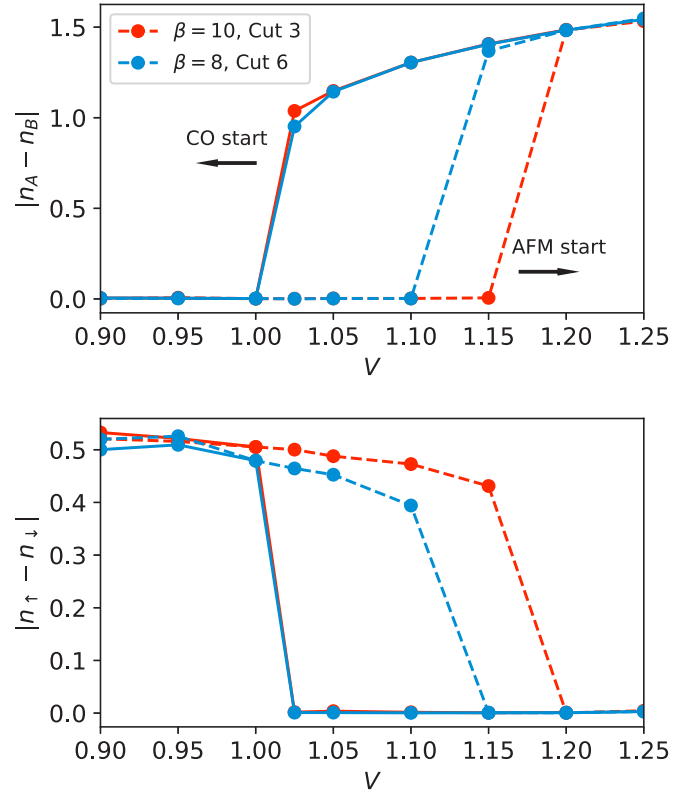


FIG. 5. Hysteresis between AFM and CO state. $U = 4t$, $\beta t = 10$ (red) and $\beta t = 8$ (blue). Top panel: CO order parameter, Δ_{CO} . Bottom panel: AFM order parameter, Δ_{AFM} . Dashed (solid) lines indicate convergence from a CO (AFM) initial guess.

region, both of these simulations converge to the same solution. In contrast, in a coexistence region both states will be stable and the two simulations will converge to different solutions.

The top panel of Fig. 5 shows the CO order parameter, while the bottom panel shows the AFM order parameter. Shown is a trace along cut 3 ($\beta t = 10$) and cut 6 ($\beta t = 8$) as a function of V . A coexistence regime starts at $V/t \sim 1$ and extends to $V/t \sim 1.2$ at the lower temperature, and shrinks as temperature increases (demonstrated by the $T/t = 1/8$ data) and eventually vanishes, see Fig. 1. The data indicates that the stable states are always only AFM or CO, and that no solutions have both finite AFM and finite CO ordering.

We also find the evidence for a small hysteresis region in the normal/CO transition shown in Fig. 6. The figure shows the converged CO order parameter resulting from two sets of simulations, at $\beta t = 5$ and $U/t = 4$. In the first set, each simulation is started with a normal state solution with a small CO offset. In the second set, each simulation is started with a CO state solution. For a narrow range of V , from about $V/t \approx 1.065$ to $V/t \approx 1.09$, these simulations reveal that both normal and CO states are stable. This indicates that at this temperature and interaction strength, the normal to charge-order phase transition is first order.

This finding is consistent with the sharp transition in energy displayed in Fig. 4, as well as previous work [49] that indicated that the normal to CO transition is continuous at

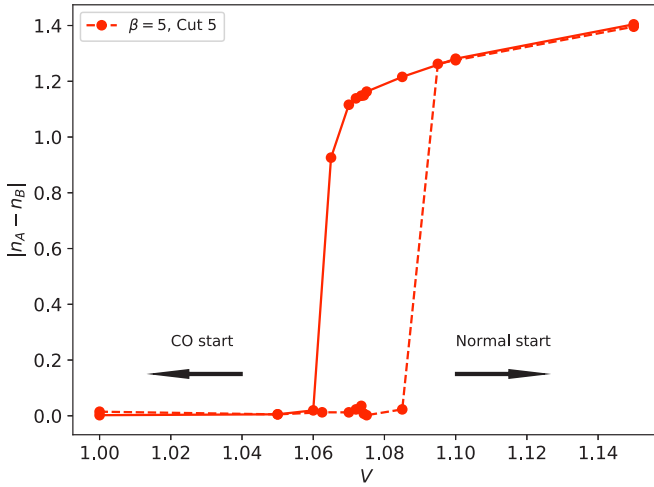


FIG. 6. Hysteresis between normal and CO states. $U = 4t$, $\beta t = 5$. The data indicate the hysteresis behavior across the transition depending on the starting solution. Shown is the converged CO order parameter, Δ_{CO} , arising from simulations started with normal solution with a small CO offset (dashed) and a CO solution (solid).

small U but sharpens as U is increased [32,52,55]. Since the hysteresis region is so narrow, we do not attempt to draw it

on our phase diagrams. All other plots in this paper dealing with the normal to CO transition display data obtained from simulations that start with a normal state solution.

F. Spectral functions

Figure 7 shows the evolution of the spectral function and self-energy across the AFM/CO phase boundary at $U = 3.5t$ and $\beta t = 10$. The first column depicts the different sublattice and spin contributions to the total spectral function, which is shown in the second column. The symmetry of the sublattice and spin components vary as described in Sec. II. At lower V , the occupied states (i.e., states with energy below $\omega = 0$) are predominantly those with spin up on the A sublattice and spin down on the B sublattice. These components are equal to each other and related to the other components (spin down on sublattice A and spin up on sublattice B) by particle-hole symmetry (i.e., $\omega \rightarrow -\omega$), as expected for an AFM state. Upon increasing V and transitioning into the CO state, the symmetry of the spectral function components change so electrons occupy the A sublattice and vacate the B sublattice, with symmetry between the up- and down-spin components.

We can use the total spectral function results to compare the energy gaps at $\omega = 0$ on either side of the AFM/CO transition. At lower V , the system is not fully gapped and is

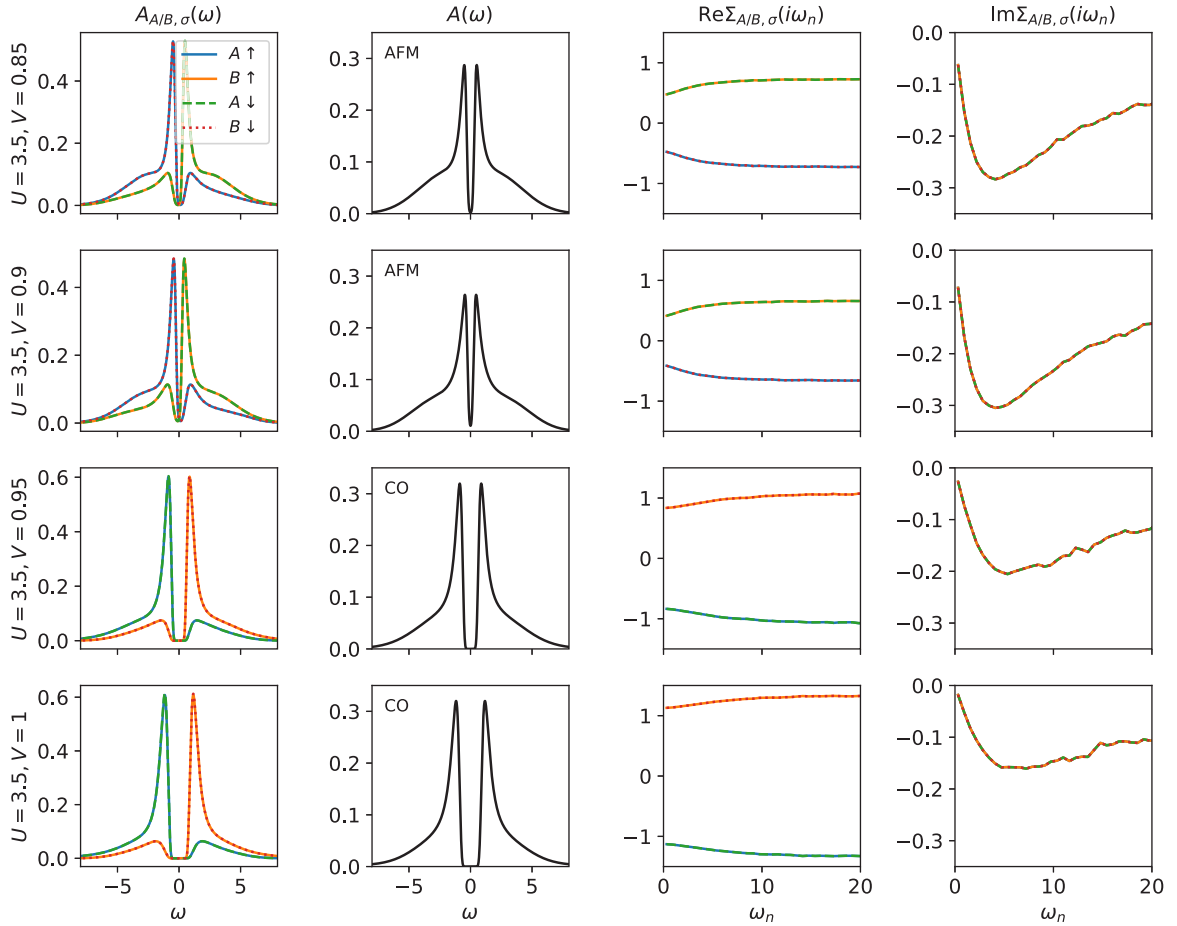


FIG. 7. Evolution of spectral functions across AFM-CO phase boundary at $U = 3.5t$ at $\beta t = 10$. First column: Spin and sublattice resolved spectral function. Second column: Local spectral function depicting the qualitative difference between the small AFM and large CO gap. Third and fourth columns: Real and imaginary parts of the Matsubara frequency self-energy.

in a metallic state with AFM order. In contrast, the CO state displays a gap immediately after the transition.

The last two columns of Fig. 7 show how the real and imaginary parts of the sublattice and spin-resolved Matsubara self-energies behave through the AFM/CO transition. The real parts switch symmetry and increase in magnitude upon entering the CO state, in agreement with the formation of a robust electronic gap. In contrast, the imaginary part of the self-energy seems to be smaller in the charge-order state than the AFM state, indicating smaller correlation effects. This behavior makes physical sense because the AFM state is dependent upon spin correlations between electrons in the two sublattices (i.e., virtual exchange hopping), whereas the CO state can be viewed as a result of classical energetics that favor a reduction in the double occupancy.

Spectral functions were obtained via the maximum entropy method, as implemented by the ALPS MAXENT software package [88,89].

IV. CONCLUSION

In conclusion, we have presented results for the 2D half-filled extended Hubbard model. Within the DCA approximation, the model exhibits both AFM and CO originating from strong electronic correlations. These orders are stable in a large part of parameter space, allowing us to probe the behavior of a physical observable in the vicinity of the phase transitions as well as deep within a phase.

We find that the nonlocal interactions, which promote screening and CO, also strongly suppress AFM. Nevertheless, there is a phase coexistence regime. Phase boundaries are consistent with a continuous transition in the case of the

normal-AFM transition, and are first order (we show hysteresis) in the case of the normal-CO and AFM-CO boundaries. A detailed analysis of the energetics, of order parameters, and of the spectral functions is provided.

Real materials that exhibit CO in the vicinity of AFM are considerably more complex than the simple extended Hubbard model. Nevertheless, there is merit in identifying model systems and nonperturbative approximations in which those phases occur in close proximity, as simple competition effects such as the one between local and nonlocal interactions here can provide general guiding principles for understanding their overall behavior.

While the exact solution of the 2D model does not support long-range ordered AFM, none of the physical compounds are idealized 2D systems. The role of a weak interlayer coupling or of other band-structure effects is mimicked by the short-ranged nature of the DCA approximation.

It would be very interesting to examine if other ordered phases, such as superconductivity, emerge in the vicinity of AFM and CO. The temperatures accessible in our systems are much too high to address this question directly, though other techniques such as a susceptibility analysis [19,90] may be employed. We therefore leave this question open for further study.

ACKNOWLEDGMENTS

This work was supported by NSF DMR-1606348. Computer time was provided via the Extreme Science and Engineering Discovery Environment (XSEDE), supported by National Science Foundation Grant Number ACI-1548562 through Allocation No. DMR130036.

- [1] E. Dagotto, *Science* **309**, 257 (2005).
- [2] M. Imada, A. Fujimori, and Y. Tokura, *Rev. Mod. Phys.* **70**, 1039 (1998).
- [3] A. Damascelli, Z. Hussain, and Z.-X. Shen, *Rev. Mod. Phys.* **75**, 473 (2003).
- [4] P. Battle, T. Gibb, and P. Lightfoot, *J. Solid State Chem.* **84**, 237 (1990).
- [5] J. M. Tranquada, J. E. Lorenzo, D. J. Buttrey, and V. Sachan, *Phys. Rev. B* **52**, 3581 (1995).
- [6] B. J. Sternlieb, J. P. Hill, U. C. Wildgruber, G. M. Luke, B. Nachumi, Y. Moritomo, and Y. Tokura, *Phys. Rev. Lett.* **76**, 2169 (1996).
- [7] B. Raveau and A. M. Seikh, *Z. Anorg. Allg. Chem.* **641**, 1385 (2015).
- [8] H. Chu, L. Zhao, A. de la Torre, T. Hogan, S. D. Wilson, and D. Hsieh, *Nat. Mater.* **16**, 200 (2017).
- [9] J. Leshen, M. Kawai, I. Giannakis, Y. Kaneko, Y. Tokura, S. Mukherjee, W.-C. Lee, and P. Aynajian, *Comm. Phys.* **2**, 36 (2019).
- [10] J. G. Bednorz and K. A. Müller, *Z. Phys. B* **64**, 189 (1986).
- [11] D. Jérôme, *Science* **252**, 1509 (1991).
- [12] W. Yu, F. Zhang, F. Zamborszky, B. Alavi, A. Baur, C. A. Merlic, and S. E. Brown, *Phys. Rev. B* **70**, 121101(R) (2004).
- [13] F. Nad and P. Monceau, *J. Phys. Soc. Jpn.* **75**, 051005 (2006).
- [14] N. Matsunaga, S. Hirose, N. Shimohara, T. Satoh, T. Isome, M. Yamamoto, Y. Liu, A. Kawamoto, and K. Nomura, *Phys. Rev. B* **87**, 144415 (2013).
- [15] H. Seo, *J. Phys. Soc. Jpn.* **69**, 805 (2000).
- [16] M. Dressel and N. Drichko, *Chem. Rev.* **104**, 5689 (2004).
- [17] R. H. McKenzie, J. Merino, J. B. Marston, and O. P. Sushkov, *Phys. Rev. B* **64**, 085109 (2001).
- [18] J. P. F. LeBlanc, A. E. Antipov, F. Becca, I. W. Bulik, G. K.-L. Chan, C.-M. Chung, Y. Deng, M. Ferrero, T. M. Henderson, C. A. Jiménez-Hoyos, E. Kozik, X.-W. Liu, A. J. Millis, N. V. Prokof'ev, M. Qin, G. E. Scuseria, H. Shi, B. V. Svistunov, L. F. Tocchio, I. S. Tupitsyn, S. R. White, S. Zhang, B.-X. Zheng, Z. Zhu, and E. Gull Simons collaboration on the many-electron problem, *Phys. Rev. X* **5**, 041041 (2015).
- [19] O. Gunnarsson, T. Schäfer, J. P. F. LeBlanc, E. Gull, J. Merino, G. Sangiovanni, G. Rohringer, and A. Toschi, *Phys. Rev. Lett.* **114**, 236402 (2015).
- [20] E. Gull, O. Parcollet, P. Werner, and A. J. Millis, *Phys. Rev. B* **80**, 245102 (2009).
- [21] E. Gull, M. Ferrero, O. Parcollet, A. Georges, and A. J. Millis, *Phys. Rev. B* **82**, 155101 (2010).
- [22] W. Wu, M. Ferrero, A. Georges, and E. Kozik, *Phys. Rev. B* **96**, 041105(R) (2017).
- [23] B.-X. Zheng, C.-M. Chung, P. Corboz, G. Ehlers, M.-P. Qin, R. M. Noack, H. Shi, S. R. White, S. Zhang, and G. K.-L. Chan, *Science* **358**, 1155 (2017).
- [24] T. O. Wehling, E. Şaşoğlu, C. Friedrich, A. I. Lichtenstein, M. I. Katsnelson, and S. Blügel, *Phys. Rev. Lett.* **106**, 236805 (2011).

- [25] P. Hansmann, T. Ayrál, L. Vaugier, P. Werner, and S. Biermann, *Phys. Rev. Lett.* **110**, 166401 (2013).
- [26] J. Solyom, *EPJ Web Conf.* **78**, 01009 (2014).
- [27] M. Schüler, M. Rösner, T. O. Wehling, A. I. Lichtenstein, and M. I. Katsnelson, *Phys. Rev. Lett.* **111**, 036601 (2013).
- [28] C. Eichstaedt, Y. Zhang, P. Laurell, S. Okamoto, A. G. Eguiluz, and T. Berlijn, *arXiv:1904.01523*.
- [29] Y. Zhang and J. Callaway, *Phys. Rev. B* **39**, 9397 (1989).
- [30] S. Fuchs, E. Gull, M. Troyer, M. Jarrell, and T. Pruschke, *Phys. Rev. B* **83**, 235113 (2011).
- [31] J. E. Hirsch, *Phys. Rev. Lett.* **53**, 2327 (1984).
- [32] M. Aichhorn, H. G. Evertz, W. von der Linden, and M. Potthoff, *Phys. Rev. B* **70**, 235107 (2004).
- [33] W. Wu and A.-M. S. Tremblay, *Phys. Rev. B* **89**, 205128 (2014).
- [34] T. Ayrál, S. Biermann, P. Werner, and L. Boehnke, *Phys. Rev. B* **95**, 245130 (2017).
- [35] T. Ayrál, S. Biermann, and P. Werner, *Phys. Rev. B* **87**, 125149 (2013).
- [36] K. J. Kapcia, S. Robaszkiewicz, M. Capone, and A. Amaricci, *Phys. Rev. B* **95**, 125112 (2017).
- [37] A. Camjayi, K. Haule, V. Dobrosavljević, and G. Kotliar, *Nat. Phys.* **4**, 932 (2008).
- [38] K. Rościszewski and A. M. Oleś, *J. Phys.: Condens. Matter* **15**, 8363 (2003).
- [39] L. Cano-Cortés, J. Merino, and S. Fratini, *Phys. Rev. Lett.* **105**, 036405 (2010).
- [40] J. Merino, *Phys. Rev. Lett.* **99**, 036404 (2007).
- [41] J. Gao and J. Wang, *J. Phys.: Condens. Matter* **21**, 485702 (2009).
- [42] A. Amaricci, A. Camjayi, K. Haule, G. Kotliar, D. Tanasković, and V. Dobrosavljević, *Phys. Rev. B* **82**, 155102 (2010).
- [43] B. Davoudi and A.-M. S. Tremblay, *Phys. Rev. B* **74**, 035113 (2006).
- [44] B. Davoudi and A.-M. S. Tremblay, *Phys. Rev. B* **76**, 085115 (2007).
- [45] B. Davoudi, S. R. Hassan, and A.-M. S. Tremblay, *Phys. Rev. B* **77**, 214408 (2008).
- [46] E. G. C. P. van Loon, A. I. Lichtenstein, M. I. Katsnelson, O. Parcollet, and H. Hafermann, *Phys. Rev. B* **90**, 235135 (2014).
- [47] D. Medvedeva, S. Isakov, F. Krien, V. V. Mazurenko, and A. I. Lichtenstein, *Phys. Rev. B* **96**, 235149 (2017).
- [48] S. Chauvin, T. Ayrál, L. Reining, and S. Biermann, *arXiv:1709.07901*.
- [49] H. Terletska, T. Chen, and E. Gull, *Phys. Rev. B* **95**, 115149 (2017).
- [50] H. Terletska, T. Chen, J. Paki, and E. Gull, *Phys. Rev. B* **97**, 115117 (2018).
- [51] D. Sénéchal, A. G. R. Day, V. Bouliane, and A.-M. S. Tremblay, *Phys. Rev. B* **87**, 075123 (2013).
- [52] M. Schüler, E. G. C. P. van Loon, M. I. Katsnelson, and T. O. Wehling, *Phys. Rev. B* **97**, 165135 (2018).
- [53] M. Jiang, U. R. Hähner, T. C. Schulthess, and T. A. Maier, *Phys. Rev. B* **97**, 184507 (2018).
- [54] A. Reymbaut, M. Charlebois, M. F. Asiani, L. Fratino, P. Sémon, G. Sordi, and A.-M. S. Tremblay, *Phys. Rev. B* **94**, 155146 (2016).
- [55] M. Schüler, E. G. C. P. van Loon, M. I. Katsnelson, and T. O. Wehling, *SciPost Phys.* **6**, 67 (2019).
- [56] G. Rohringer, H. Hafermann, A. Toschi, A. A. Katanin, A. E. Antipov, M. I. Katsnelson, A. I. Lichtenstein, A. N. Rubtsov, and K. Held, *Rev. Mod. Phys.* **90**, 025003 (2018).
- [57] P. Werner and M. Casula, *Condens. Matter* **28**, 383001 (2016).
- [58] P. Sun and G. Kotliar, *Phys. Rev. B* **66**, 085120 (2002).
- [59] A. N. Rubtsov, M. I. Katsnelson, and A. I. Lichtenstein, *Ann. Phys.* **327**, 1320 (2012).
- [60] E. G. C. P. van Loon, M. Schüler, M. I. Katsnelson, and T. O. Wehling, *Phys. Rev. B* **94**, 165141 (2016).
- [61] E. A. Stepanov, L. Peters, I. S. Krivenko, A. I. Lichtenstein, M. I. Katsnelson, and A. N. Rubtsov, *npj Quantum Mater.* **3**, 54 (2018).
- [62] E. A. Stepanov, A. Huber, A. I. Lichtenstein, and M. I. Katsnelson, *Phys. Rev. B* **99**, 115124 (2019).
- [63] M. H. Hettler, A. N. Tahvildar-Zadeh, M. Jarrell, T. Pruschke, and H. R. Krishnamurthy, *Phys. Rev. B* **58**, R7475 (1998).
- [64] T. A. Maier, M. Jarrell, T. Pruschke, and M. Hettler, *Rev. Mod. Phys.* **77**, 1027 (2005).
- [65] N. D. Mermin and H. Wagner, *Phys. Rev. Lett.* **17**, 1133 (1966).
- [66] M. Jarrell, T. Maier, C. Huscroft, and S. Moukouri, *Phys. Rev. B* **64**, 195130 (2001).
- [67] T. A. Maier, M. Jarrell, T. C. Schulthess, P. R. C. Kent, and J. B. White, *Phys. Rev. Lett.* **95**, 237001 (2005).
- [68] A. I. Lichtenstein and M. I. Katsnelson, *Phys. Rev. B* **62**, R9283(R) (2000).
- [69] D. Sénéchal, *arXiv:0806.2690*.
- [70] A. Foley, S. Verret, A. M. S. Tremblay, and D. Sénéchal, *Phys. Rev. B* **99**, 184510 (2019).
- [71] L. Fratino, P. Sémon, M. Charlebois, G. Sordi, and A.-M. S. Tremblay, *Phys. Rev. B* **95**, 235109 (2017).
- [72] A. Georges, G. Kotliar, W. Krauth, and M. J. Rozenberg, *Rev. Mod. Phys.* **68**, 13 (1996).
- [73] R. Arita, S. Onari, K. Kuroki, and H. Aoki, *Phys. Rev. Lett.* **92**, 247006 (2004).
- [74] E. Gull, P. Werner, O. Parcollet, and M. Troyer, *Europhys. Lett.* **82**, 57003 (2008).
- [75] E. Gull, P. Staar, S. Fuchs, P. Nukala, M. S. Summers, T. Pruschke, T. C. Schulthess, and T. Maier, *Phys. Rev. B* **83**, 075122 (2011).
- [76] E. Gull, A. J. Millis, A. I. Lichtenstein, A. N. Rubtsov, M. Troyer, and P. Werner, *Rev. Mod. Phys.* **83**, 349 (2011).
- [77] See Supplemental Material at <http://link.aps.org/supplemental/10.1103/PhysRevB.99.245146> for the behavior of real part of the self-energy at frequency going to infinity for all the cuts shown in Fig. 1.
- [78] J. Merino and R. H. McKenzie, *Phys. Rev. Lett.* **87**, 237002 (2001).
- [79] U. Wolff, *Nucl. Phys. B* **225**, 391 (1983).
- [80] X.-Z. Yan, *Phys. Rev. B* **48**, 7140 (1993).
- [81] R. A. Bari, *Phys. Rev. B* **3**, 2662 (1971).
- [82] A. A. Rusakov, J. J. Phillips, and D. Zgid, *J. Chem. Phys.* **141**, 194105 (2014).
- [83] K. Haule, *Phys. Rev. B* **75**, 155113 (2007).
- [84] E. Gull, P. Werner, X. Wang, M. Troyer, and A. J. Millis, *Europhys. Lett.* **84**, 37009 (2008).
- [85] H. Park, K. Haule, and G. Kotliar, *Phys. Rev. Lett.* **101**, 186403 (2008).

- [86] S. Fuchs, E. Gull, L. Pollet, E. Burovski, E. Kozik, T. Pruschke, and M. Troyer, [Phys. Rev. Lett.](#) **106**, 030401 (2011).
- [87] J. P. F. LeBlanc and E. Gull, [Phys. Rev. B](#) **88**, 155108 (2013).
- [88] R. Levy, J. LeBlanc, and E. Gull, [Comput. Phys. Commun.](#) **215**, 149 (2017).
- [89] M. Wallerberger, S. Isakov, A. Gaenko, J. Kleinhenz, I. Krivenko, R. Levy, J. Li, H. Shinaoka, S. Todo, T. Chen, X. Chen, J. P. F. LeBlanc, J. E. P. P. Paki, H. Terletska, M. Troyer, and E. Gull, [arXiv:1811.08331](#).
- [90] X. Chen, J. P. F. LeBlanc, and E. Gull, [Phys. Rev. Lett.](#) **115**, 116402 (2015).